Conductance and gating effects at sputtered oxide interfaces

Yin, C.

1

Introduction

1

1.1. Complex oxides

The semiconductor-based transistor launched a revolution in electronics when it was invented at Bell lab in 1947. Silicon integrated circuits are the foundation of basically everything we take for granted now in our daily life. Nevertheless, silicon electronics faces a challenge: the latest transistor is only 7 nm wide, and further shrinking the size would lead to unstable behavior. This challenge requires redesign and more advanced devices, or looking for alternative materials to silicon.

Complex oxide materials offer scientists and engineers a theme park of new physics. They exhibit a wide range of novel functionalities which cannot be achieved in conventional semiconductors, including colossal magnetoresistance, high-temperature superconductivity, metal-insulator transitions, and multiferroicity [1]. A complex oxide contains oxygen and at least one other element, which is usually from the transition metal group. In many complex oxides, the electrons are strongly correlated [2, 3]. Their rich phenomena arise from the complex interplay between the charge, orbital, lattice and spin degrees of freedom, as illustrated in Fig. 1.1(a).

In the complex oxides family, perovskites with the chemical formula ABO_3 have received a remarkable amount of attention. The crystal structure of an ideal perovskite oxide is sketched in Fig. 1.1(b). This structure possesses an extraordinary chemical flexibility – most of the elements found in the periodic table can be placed on the A or B sites [4]. The ideal cubic structure is rare in nature and usually undergoes symmetry-lowering distortions depending on the size of the A and B cations. The deviation from the ideal

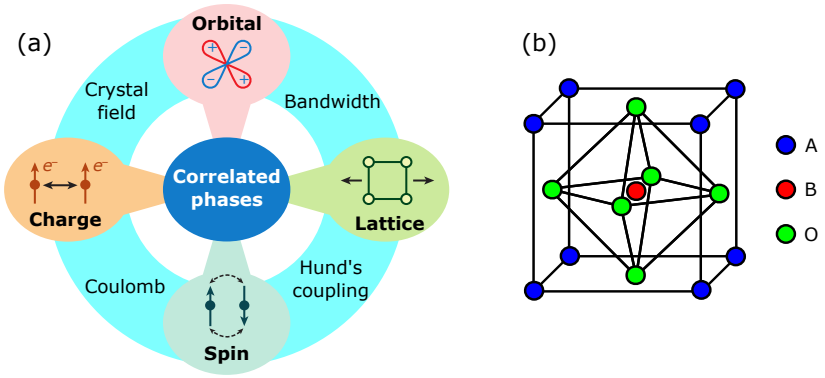

Figure 1.1: (a) The interplay between charge, orbital, lattice and spin degrees of freedom gives rise to correlated phases in transition metal oxides. Image reprinted from Ref. [3]. (b) The crystal structure of an ideal perovskite oxide, ABO_3. The blue, red and green spheres represent the A, B, and O atoms, respectively.

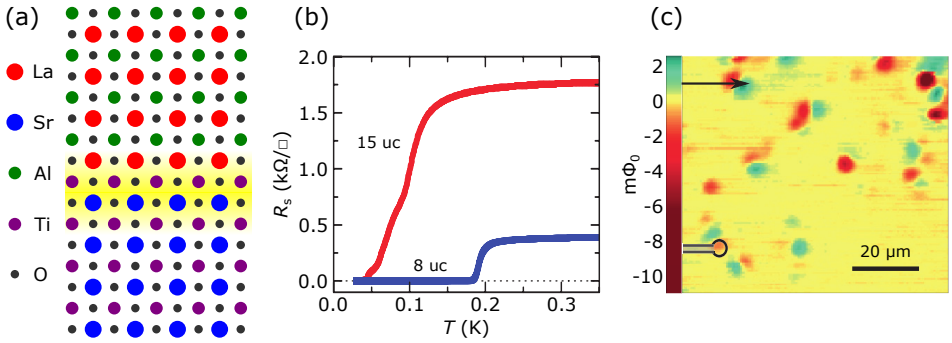

Figure 1.2: (a) Sketch of the $LaAlO_3/SrTiO_3$ interface. The yellow area represent the 2DES. (b) Sheet resistance (R_s) as a function of temperature of samples with $LaAlO_3$ thicknesses of 8 and 15 unit cells, showing the occurrence of superconductivity. Image adapted from Ref. [6]. (c) Scanning SQUID image mapping the ferromagnetic order in $LaAlO_3/SrTiO_3$. The inset shows the SQUID pick-up loop for sensing magnetic flux and the arrow denotes the fast scan axis and the SQUID orientation. Image adapted from Ref. [7].

structure can be quantified by the Goldschmidt tolerance factor [5]

$$t = \frac{r_A + r_O}{\sqrt{2}(r_B + r_O)}, \tag{1.1}$$

where r_A, r_B and r_O are the ionic radii of the A, B and O ions, respectively. The richness of physical properties exhibited by perovskite oxides is closely related to the diversity of structural distortions in these materials.

1.2. $LaAlO_3/SrTiO_3$ heterostructures

In his Nobel lecture, Herbert Kroemer coined the famous phrase that "the interface is the device" [8]. During the past decades, advancements in thin film growth technology have enabled the fabrication of oxide heterostructures with atomic precision. A landmark work appeared in 2004, in which Ohtomo and Hwang reported a high-mobility two-dimensional electron system (2DES) at the interface between $LaAlO_3$ and $SrTiO_3$ [9]. A sketch of the $LaAlO_3/SrTiO_3$ interface is given in Fig. 1.2(a). Both materials are band insulators in bulk, with band gaps of 5.6 eV and 3.25 eV for $LaAlO_3$ and $SrTiO_3$, respectively. Therefore the discovery of this conductive interface with a mobility exceeding 10^4 cm^2/Vs is indeed remarkable. Ever since then the $LaAlO_3/SrTiO_3$ heterostructure has generated an enormous amount of research interest in the oxide community.

In the past 15 years, scientists have observed many other intriguing properties beyond conductivity at the $LaAlO_3/SrTiO_3$ interface, such as superconductivity, magnetism and even their coexistence. Superconductivity was first reported by Reyren *et al.* [6] as shown in Fig. 1.2(b). They found that the superconducting transition temperature is

about 200 mK and the thickness of the superconducting layer is approximately 10 nm.

$LaAlO_3$ and $SrTiO_3$ are both non-magnetic materials. It was quite surprising when Brinkman *et al.* [10] first reported magnetism at the $LaAlO_3/SrTiO_3$ interface. They observed a Kondo-like resistance minimum and a hysteretic magnetoresistance, although the hysteresis was later found to be a measurement artifact. To date, signatures of magnetism have been observed by many different measurement techniques, such as superconducting quantum interference device (SQUID) [11], magnetic torque magnetometry [12], scanning SQUID [7, 13, 14] as shown in Fig. 1.2(c), x-ray magnetic circular dichroism [15, 16], magnetic force microscopy [17] and magnetotransport measurement [18–20]. However, the reported results are inconsistent and a convincing physical picture for the origin of the magnetism is still lacking.

1.3. Mechanisms for interfacial conduction

The physical mechanism responsible for the formation of the 2DES at the $LaAlO_3/SrTiO_3$ interface has been a highly debated topic since its discovery. A proper explanation which can cover all the experimental observations is still lacking. Proposed mechanisms basically fall into two categories, namely intrinsic and extrinsic mechanisms. The intrinsic mechanism considers the polar discontinuity between the polar $LaAlO_3$ and the non-polar $SrTiO_3$. The extrinsic mechanisms involve the roles of different defects which are formed during film growth. In this section, we introduce these mechanisms and briefly discuss their limitations. More detailed information can be found in recent review articles [21, 22].

1.3.1. Intrinsic mechanism: polar discontinuity

In their seminal paper, Ohtomo and Hwang proposed that the polar discontinuity at the $LaAlO_3/SrTiO_3$ interface is the dominant mechanism for conductivity [9]. This mechanism was later discussed in detail by Nakagawa *et al.* [23] in the polar catastrophe model, which is illustrated in Fig. 1.3. In the [001] direction, a perovskite oxide, ABO_3, can be considered as alternating stacks of AO and BO_2 planes. $SrTiO_3$ consists of neutral $Sr^{2+}O^{2-}$ and $Ti^{4+}O_2^{4-}$ planes, whereas $LaAlO_3$ consists of charged $La^{3+}O^{2-}$ and $Al^{3+}O_2^{4-}$ planes, carrying formal $+1$ and -1 charges, respectively. Depending on $SrTiO_3$ surface termination, two types of interface can be obtained: the LaO/TiO_2 interface (Fig. 1.3(a)) and the AlO_2/SrO interface (Fig. 1.3(b)). In both cases, the alternating net charges (ρ) in LaO and AlO_2 planes produce an electric field (E), leading to a diverging electric potential (V) as the thickness of $LaAlO_3$ layer increases, which is known as the polar catastrophe [24, 25]. In order to prevent the catastrophe, the system undergoes different types of interfacial reconstructions. For the LaO/TiO_2 interface, an electronic reconstruction

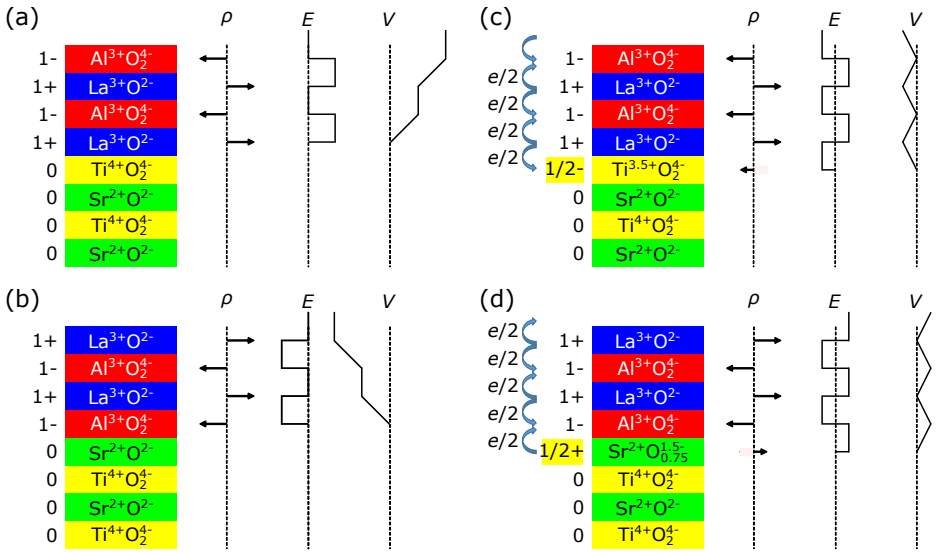

Figure 1.3: An illustration of the polar catastrophe model for atomically abrupt (001) interfaces between $LaAlO_3$ and $SrTiO_3$. (a) The unreconstructed interface has neutral (001) planes in $SrTiO_3$, but the (001) planes in $LaAlO_3$ have alternating net charges (ρ). If the interface plane is LaO/TiO_2, this produces a non-negative electric field (E), leading in turn to an electric potential (V) that diverges with thickness. (b) If the interface is instead placed at the AlO_2/SrO plane, V diverges negatively. (c) The divergence catastrophe at the LaO/TiO_2 interface can be avoided if half an electron is added to the last TiO_2 plane. This produces an interface dipole that causes E to oscillate about 0 while V remains finite. (d) The divergence for the AlO_2/SrO interface can also be avoided by removing half an electron from the SrO plane in the form of oxygen vacancies. Image adapted from Ref. [23].

occurs by transferring half an electron per unit cell from $LaAlO_3$ to $SrTiO_3$ (Fig. 1.3(c)), resulting in an n-type interface where half of the Ti^{4+} ions becoming Ti^{3+}. In the same manner, a p-type interface should be formed for the AlO_2/SrO interface. This can be achieved through an atomic reconstruction, namely oxygen vacancies formation in the SrO layer (Fig. 1.3(d)).

A robust support for the polar catastrophe model is that interfacial conduction only occurs when the $LaAlO_3$ layer exceeds a critical thickness of 4 unit cells [26]. At the critical point, the valence band at the $LaAlO_3$ surface crosses the $SrTiO_3$ conduction band at the interface, resulting in the charge transfer. Therefore, altering the polarization of the $LaAlO_3$ layer should alter the critical thickness. This has been experimentally demonstrated by Reinle-Schmitt *et al.* [27] by diluting $LaAlO_3$ with $SrTiO_3$, forming $(LaAlO_3)_x(SrTiO_3)_{1-x}/SrTiO_3$ interfaces. The critical thickness increases with decreasing x.

On the other hand, there are a number of experimental observations that the polar

catastrophe model fails to explain. First, it predicts a *p*-type interface for SrO-terminated $SrTiO_3$, however this interface is always found to be insulating [9]. Second, the model requires a charge transfer of half an electron per unit cell, which correspond to a carrier density of 3×10^{14} cm^{-2}. But experimentally measured carrier densities are usually one order of magnitude lower [28–30]. Third, the core-level shift of $LaAlO_3$ measured by x-ray photoemission spectroscopy is much smaller than the value predicted by the polar catastrophe model [31–35]. Moreover, the shift is independent of the $LaAlO_3$ thickness, which is against the electronic reconstruction picture involving a cumulative shift of the $LaAlO_3$ valence band above the $SrTiO_3$ conduction band [34]. Fourth, conductivity has been also observed at interfaces where polar discontinuity does not exist, such as amorphous $LaAlO_3$ on $SrTiO_3$ (001) [36] and crystalline $LaAlO_3$ on $SrTiO_3$ (110) [37, 38].

1.3.2. Extrinsic mechanisms: roles of defects

It is important to note that the polar catastrophe model considers an ideal $LaAlO_3/SrTiO_3$ interface as shown in Fig. 1.4(a). However, it is practically impossible to obtain such a defect-free interface. A real interface contains various types of defects, whose influences on interfacial conduction should not be neglected [39]. Here, we discuss three main defect-driven mechanisms.

The first extrinsic mechanism for generating carriers is the formation of oxygen vacancies as depicted in Fig. 1.4(b). Oxygen vacancies are the most abundant defects in $SrTiO_3$, which greatly affect the electronic, magnetic and optical properties. They can be easily introduced by annealing $SrTiO_3$ in a reducing atmosphere, and give rise to even superconductivity [40]. In $LaAlO_3/SrTiO_3$ heterostructures, the concentration of oxygen vacancies depends on the temperature and oxygen pressure during growth [41–43]. They can be significantly removed by post oxygen annealing [44–46]. Using a conducting-tip atomic force microscope, Basletic *et al.* [44] directly measured the thickness of the 2DES to be ~ 7 nm after high oxygen pressure annealing. On the other hand, theoretical works have predicted that oxygen vacancies formed at the $LaAlO_3$ surface can also be a possible source of electrons for the 2DES [47, 48].

The second extrinsic source of electrons is La/Sr intermixing as shown in Fig. 1.4(c). It has been known that La-doped $SrTiO_3$ is metallic due to the replacement of Sr^{2+} by La^{3+} [49]. La/Sr intermixing at the $LaAlO_3/SrTiO_3$ interface has been experimentally observed by electron energy loss spectroscopy [23], surface x-ray diffraction [50] and medium-energy ion spectroscopy [51].

The third extrinsic origin for interfacial conduction is $LaAlO_3$ stoichiometry. To date, $LaAlO_3/SrTiO_3$ heterostructures are commonly prepared by pulsed laser deposition (PLD). A fundamental premise that justifies the use of PLD is the stoichiometric transfer of materials from the target to the film. However, Ohnishi *et al.* have shown that obtaining

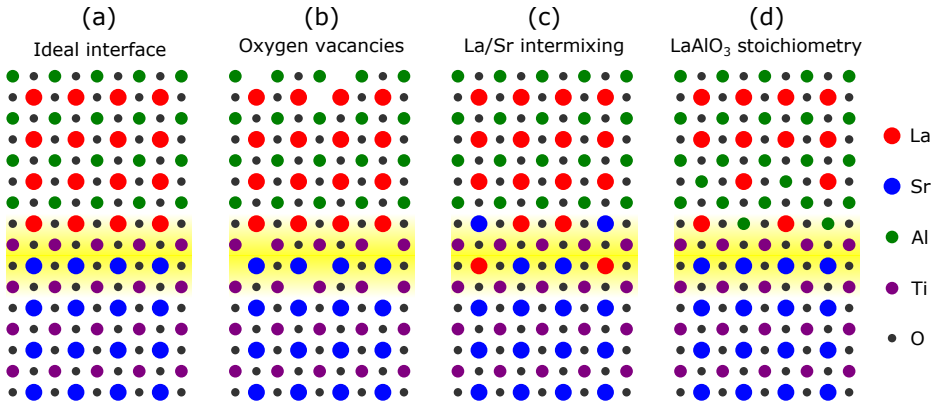

Figure 1.4: (a) An ideal $LaAlO_3/SrTiO_3$ interface. (b)-(d) Illustrations of extrinsic defect-driven mechanisms. (b) Oxygen vacancies formed either in $SrTiO_3$ at the interface or at the $LaAlO_3$ surface. (c) La/Sr intermixing at the interface. (d) Cation stoichiometry in $LaAlO_3$ films. Image shows the Al-rich case. The yellow area in each image represent the 2DES.

a stoichiometric film from PLD is a rare case rather than routine [52, 53]. It has been reported by several PLD groups that a slight variation in the growth parameters modifies the cation stoichiometry of $LaAlO_3$ films, resulting in a dramatic change in the interfacial conductivity [54–56]. The importance of $LaAlO_3$ stoichiometry has also been addressed by other growth techniques. Dildar *et al.* [57, 58] used on-axis sputtering to grow $LaAlO_3$ films. In order to prevent backsputtering effect, they used high oxygen pressures (typically 1 mbar). The $LaAlO_3$ films were found to be La-rich ($La/Al \approx 1.07$) and the interfaces were insulating. Warusawithana *et al.* [59] used molecular beam epitaxy (MBE). The stoichiometry of the $LaAlO_3$ films were gradually changed by finely tuning the La and Al fluxes. The interesting outcome is that interfacial conduction can only be observed in Al-rich samples ($La/Al \leqslant 0.97$) as illustrated in Fig. 1.4(d). Their further density functional theory (DFT) calculations showed different roles of defects in the polar catastrophe model. In Al-rich samples, Al can fill La vacancies without changing the net charge of the (001) planes. The electronic reconstruction can still transfer electrons to the interface. In La-rich samples, however, La can not substitute for Al, resulting in the formation of Al_2O_3-vacancy complexes which prohibits the charge transfer.

1

1.4. Electrostatic gating of $LaAlO_3/SrTiO_3$ heterostructures

The main focus of this thesis is electrostatic gating of the $LaAlO_3/SrTiO_3$ heterostructures. In this section, we first introduce the band structure at the $LaAlO_3/SrTiO_3$ interface and then discuss the main geometrical configurations for electrostatic gating and the major experimental observations.

1.4.1. Band structure at the $LaAlO_3/SrTiO_3$ interface

$SrTiO_3$ is a band insulator, where the indirect band gap energy is 3.25 eV and the direct band gap energy is 3.75 eV [60]. The conduction band of $SrTiO_3$ is dominated by the Ti $3d$ orbitals, while the valence band is composed of the O $2p$ orbitals. Fig. 1.5 shows the energy levels of the Ti $3d$ orbitals in various environments without considering the effect of atomic spin-orbit (SO) coupling. The $3d$ orbitals (d_{xy}, d_{yz}, d_{xz}, $d_{x^2-y^2}$ and $d_{3z^2-r^2}$) of an isolated Ti atom (spherical symmetry) is five-fold degenerate, which is labeled by the angular momentum $L = 2$. Once the Ti is surrounded by the oxygen octahedron (cubic symmetry, O_h point group), the $3d$ orbitals are split into a higher-energy doublet (e_g states) and a lower-energy triplet (t_{2g} states). Below 105 K, $SrTiO_3$ undergoes a ferroelastic transition from cubic to tetragonal symmetry (D_{4h} point group), which slightly shift the d_{xy} state higher in energy relative to the d_{yz} and d_{xz} states. Upon forming the $LaAlO_3/SrTiO_3$ interface, the breaking of inversion symmetry further reduces the symmetry of the system to the C_{4v} point group. This does not give rise to additional lifting of degeneracy, but completely modifies the sign and amplitude of the splittings between in-plane and out-of-plane orbitals of the e_g and the t_{2g} states. Salluzzo *et al.* [16, 61] experimentally measured the splitting energies of the e_g and the t_{2g} states to be ~100 meV and ~50 meV, respectively. The resulting t_{2g} bands are plotted in Fig. 1.5(e). When atomic SO coupling, as shown in Fig. 1.5(f), is taken into account, the combination of broken inversion symmetry and atomic SO coupling gives rise to a more complicated band splitting, as depicted in Fig. 1.5(g), which is responsible for the Rashba effect. This will be discussed further in Chapter 5.

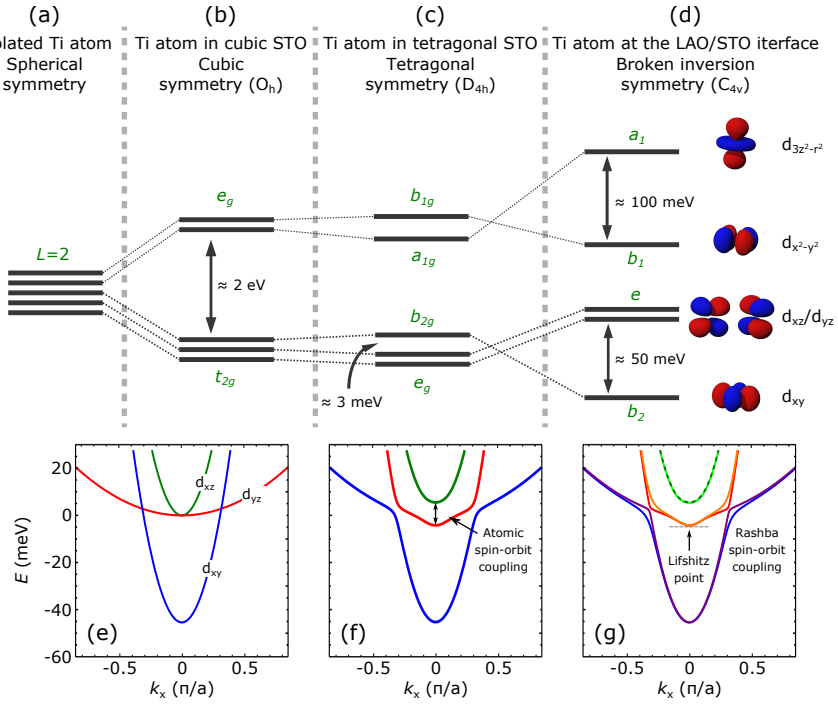

Figure 1.5: Ti electronic level structure at the $LaAlO_3/SrTiO_3$ interface. (a) The $3d$ orbitals of an isolated Ti atom are five-fold degenerate. (b) Once the Ti is surrounded by the oxygen octahedron, the orbitals are split into the e_g states and the t_{2g} states. (c) Below 105 K, $SrTiO_3$ changes from cubic to tetragonal symmetry, which slightly lifts the orbit degeneracy. (d) Upon forming the $LaAlO_3/SrTiO_3$ interface, the breaking of inversion symmetry results in larger splittings of the the e_g states and the t_{2g} states. This leads to different d-bands. Images adapted from Ref. [62]. (e)-(g) Effective three-band model at the $LaAlO_3/SrTiO_3$ interface. (e) Spin-degenerate t_{2g} bands. (f) The t_{2g} bands with atomic SO coupling included. The three bands are still double degenerate. (g) The t_{2g} bands with atomic SO coupling and inversion asymmetry included. Maximum Rashba spin splitting is at the crossing point of the d_{xy} and $d_{xz,yz}$ orbitals. The Lifshitz point is at the bottom of the $d_{xz,yz}$ bands [63]. Images adapted from Ref. [64].

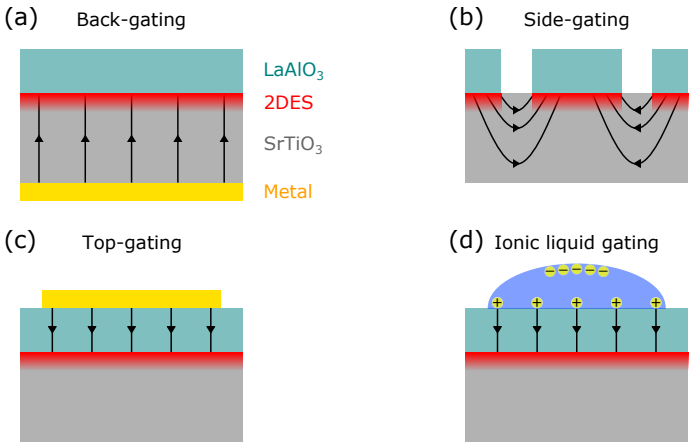

Figure 1.6: Illustrations of different geometrical configurations for $LaAlO_3/SrTiO_3$ field-effect devices. (a) Back-gating. (b) Side-gating. (c) Top-gating. (d) Ionic liquid gating. The black lines represent electric field lines induced by an external gate voltage. The legend in (a) applies to all panels.

1.4.2. Electric-field effects in $LaAlO_3/SrTiO_3$ heterostructures

Semiconducting field-effect transistors (FETs) are the workhorses of modern electronics [65]. Thus the capability of controlling the physical properties of novel materials by applying an external electric field is of crucial importance for device applications. A typical semiconductor FET consists of source and drain terminals, a conducting channel between them, and a gate terminal [66, 67]. The channel and gate electrode are separated by an insulating dielectric, forming a parallel plate capacitor. Applying a voltage across this capacitor induces charges into the channel and therefore modulates its conductance.

For the $LaAlO_3/SrTiO_3$ heterostructures, there are three main geometrical configurations for field-effect devices, namely back-gating [26], side-gating [68], and top-gating [69] as shown in Fig. 1.6(a)-(c). Ionic liquid gating, as shown in Fig. 1.6(d), belongs to the top-gating configuration, but the channel and gate electrode are covered by a drop of ionic liquid, forming an electric double layer [70]. In the past decade, an enormous number of fascinating gate-tunable effects have been achieved at the $LaAlO_3/SrTiO_3$ interface by employing different geometries.

Among the possible options, the back-gating geometry is the most widely used one. In this configuration, the gate voltage is applied across the $SrTiO_3$ substrate. The reported gate-tunable effects include insulator to metal transitions [26], insulator to superconductor transitions [71], Rashba spin-orbit coupling [18, 72–76], Shubnikov – de Haas oscillations [30, 77, 78], and the Lifshitz transition [63]. It should be noted that theses effects basically depend on the carrier density, therefore they can be modulated by

other geometries as well.

The side-gating geometry was first developed by the group of J. Levy using conductive atomic force microscopy lithography, which enables an easy writing and erasing of nanoscale structures [68]. Equipped with this technique, they were able to fabricate single-electron transistors [79, 80], control ferromagnetism at room temperature [17], and realize quantized ballistic transport [81] at the $LaAlO_3/SrTiO_3$ interface. Recently, Monteiro *et al.* fabricated side-gating devices using electron-beam lithography and realized gate-tunable Josephson junctions [82].

The top-gating geometry works in a similar way as the back-gating counterpart, but the insulating dielectric is the $LaAlO_3$ overlayer. Compared with back-gating, the big advantage of top-gating is that it requires very low voltages to achieve sizeable gating effects [83–90]. However, the device fabrication process is very complicated which is due to the requirement of multiple aligned lithography steps [91].

Ionic liquid gating is able to achieve a charge transfer that is two orders of magnitude larger than conventional FETs [92]. This technique has been used to induce or modify superconductivity in ZrNCl [93], $SrTiO_3$ [94], $KTaO_3$ [95], MoS_2 [96], $La_{2-x}Sr_xCuO_4$ [97], and $YBa_2Cu_3O_{7-x}$ [98]. It has also been employed to modulate physical properties at the $LaAlO_3/SrTiO_3$ interface [70, 99, 100]. Lin *et al.* [70] have observed a gate-tunable Kondo effect and Zeng *et al.* [99] have obtained an electron mobility up to 19 380 cm^2/Vs.

1.5. Outline of this thesis

This thesis is concerned with the fabrication of conducting interfaces made by sputter – growing thin layers of $LaAlO_3$ on $SrTiO_3$, and with studying their magnetotransport properties under the influence of an electric field. The thesis is structured as follows:

• **Chapter 2** provides detailed information of the experimental setups. We start with an introduction to sputter deposition, which is followed by a description of the 90° off-axis sputtering system. Then, we introduce the sample fabrication process, including substrate preparation, thin film deposition, and Hall bar device fabrication. Finally, we discuss the sample characterization techniques, such as atomic force microscopy, x-ray diffraction, and magnetotransport measurements.

• **Chapter 3** presents the growth of high quality epitaxial $LaAlO_3$ films on $SrTiO_3$ (001) substrates by 90° off-axis sputtering. First we show the optimization of the growth parameters. Then we demonstrate the tuning of interfacial conductance in $LaAlO_3/SrTiO_3$ by varying the sputtering pressure.

• **Chapter 4** focuses on the electron trapping effect in back-gated $LaAlO_3/SrTiO_3$. By combining magnetotransport measurements and self-consistent Schrödinger-Poisson calculations, we identify the relation between the amount of trapped electrons and the

gate voltage as well as the spatial distribution of the trapped electrons. We demonstrate that an earlier proposed thermal escape mechanism provides a misleading physical picture, and we propose a new mechanism.

• **Chapter 5** demonstrates the tuning of Rashba spin-orbit coupling in back-gated $LaAlO_3/SrTiO_3$. We aim to clarify the inconsistent dependence of Rashba effect on gate voltage in experiments, and examine the theoretical predictions. We trigger the Lifshitz transition multiple times by carefully tuning the gate voltage. By analyzing the weak antilocalization effect of the magnetoresistance, we show that the maximum Rashba effect occurs when the Fermi energy is near the Lifshitz point.

• **Chapter 6** studies the effect of $LaAlO_3$ thickness on the transport properties in $LaAlO_3/SrTiO_3$ when using ionic liquid gating. We demonstrate that the physical properties at the interface are dominated by the intrinsic interactions rather than the $LaAlO_3$ thickness. We present a Kondo effect, which is enhanced while increasing the gate voltage. We also show a gate-tunable and temperature-dependent anomalous Hall effect, which always emerges near the Kondo temperature.

• **Appendix A** provides a step-by-step description of the self-consistent Schrödinger-Poisson calculations performed for Chapter 4.